Joule

CellPress

Article

High carbon efficiency in CO-to-alcohol electroreduction using a CO reservoir

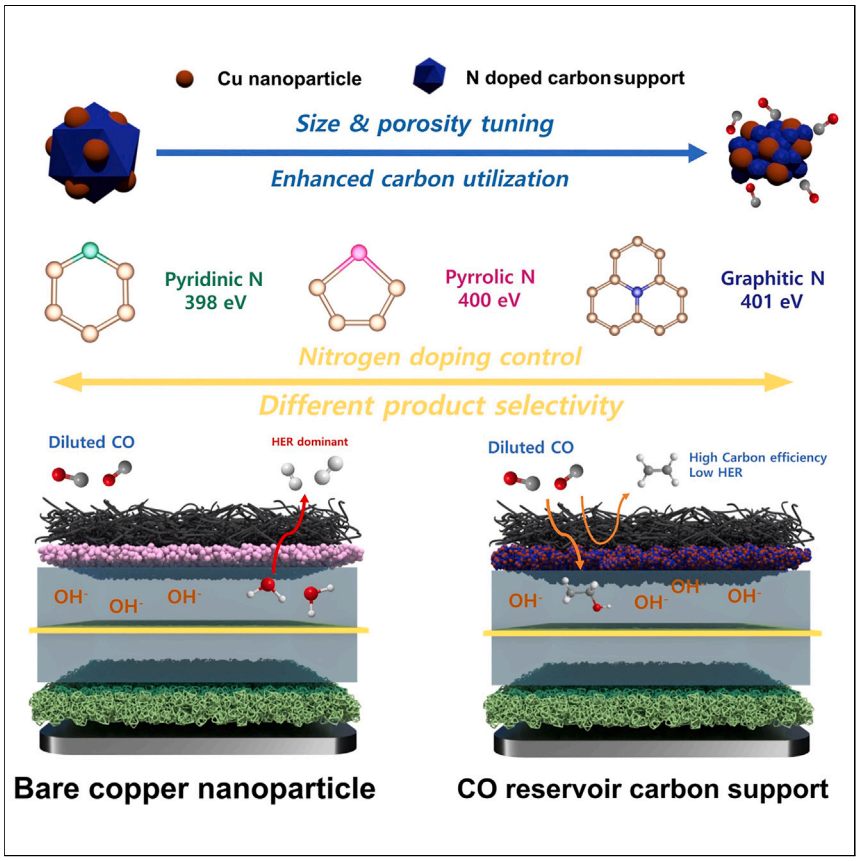

Microporous carbon nanoparticles, designed and synthesized with diverse particle sizes, porosity, and n-doping ratio, aim to maximize carbon utilization and ethanol production in CO reduction electrolysis by incorporating a heterojunction carbon reservoir catalyst.

Sungjin Park, Ivan Grigioni, Tartela Alkayyali, ..., Dongha Kim, David Sinton, Edward Sargent

dave.sinton@utoronto.ca (D.S.)
ted.sargent@utoronto.ca (E.S.)

Highlights

Optimized carbon support enables high C_{2+} selectivity in CO-deficient settings

Adjusting n-doping in carbon support controls alcohol selectivity

Electrochemical studies predict CO availability near catalysts in CO-deficient feed

Upholding carbon efficiency and selectivity cuts energy demand for C_{2+} products

Park et al., Joule 7, 1–14
October 18, 2023
https://doi.org/10.1016/j.joule.2023.08.001

Please cite this article in press as: Park et al., High carbon efficiency in CO-to-alcohol electroreduction using a CO reservoir, Joule (2023), https://doi.org/10.1016/j.joule.2023.08.001

Joule

CellPress

Article

High carbon efficiency in CO-to-alcohol electroreduction using a CO reservoir

Sungjin Park,[1,5] Ivan Grigioni,[1,2,5] Tartela Alkayyali,[4,5] Byoung-Hoon Lee,[1] Jiheon Kim,[1] Erfan Shirzadi,[1] Roham Dorakhan,[1] Geonhui Lee,[1] Jehad Abed,[1] Filippo Bossola,[3] Eui Dae Jung,[1] Yongxiang Liang,[1] Mi Gyoung Lee,[1] Ali Shayesteh Zeraati,[1] Dongha Kim,[1] David Sinton,[4,*] and Edward Sargent[1,6,*]

SUMMARY

The electrochemical CO_2 reduction reaction (CO_2RR) has progressed but suffers an energy penalty from CO_2 loss due to carbonate formation and crossover. Cascade CO_2 to CO conversion followed by CO reduction addresses this issue, but the combined figures of carbon efficiency (CE), energy efficiency (EE), selectivity, and stability require improvement. We posited that increased CO availability near active catalytic sites could maintain selectivity even under CO-depleted conditions. Here, we present a heterojunction carbon reservoir catalyst (CRC) architecture that combines copper nanoparticles with porous carbon nanoparticles. The pyridinic and pyrrolic functionalities of CRC can absorb CO enabling high CE under CO-depleted conditions. With CRC catalyst, we achieve ethanol FE and CE of 50% and 93% (CE*Faradaic efficiency [FE] = 47%) in flow cell at 200 mA cm^{-2}, fully doubling the best prior CE*FE to ethanol. In membrane electrode assembly (MEA) system, we show sustained efficiency over 85 h at 100 mA cm^{-2}.

CONTEXT & SCALE

Electrochemical reduction of CO_2 and CO provides ways to produce added-value chemicals, and the potential to achieve carbon neutrality when powered with renewable electricity. Efficient conversion of CO_2 and CO is paramount to making these approaches sustainable and cost-competitive compared with traditional fossil-energy-based ones. We report a catalyst design strategy where a CO-capturing component provides catalytic copper with a high local concentration of CO even at a conversion rate close to unity (above 90%), preventing other parasitic reactions and providing control over the product selectivity.

INTRODUCTION

The electroproduction of alcohols such as ethanol and propanol from CO_2 can potentially provide low-carbon-intensity fuels and platform chemicals. Toward this goal, it will be important to continue to improve carbon efficiency (CE, the fraction of CO_2, and CO converted into desired products in a single pass), Faradaic efficiency (FE, the selectivity to specific products), and energy efficiency (EE). System design and selective carbon-efficient catalysts are required to address these challenges.[1]

In gas-phase electrolyzers, the catalyst layer (CL) is adjacent to the catholyte and gas flow channel, forming a three-phase boundary (Figures 1A–1D). The reactant gas diffuses into the porous gas-diffusion layer (GDL) and reaches the electrocatalytic active sites in the CL. The water-based electrolyte acts as the proton source, which can react with electrons and lead to C-products. These systems can realize CO_2 reduction reaction (CO_2RR) and CO reduction reaction (CORR) at high reaction rates (above 100 mA cm^{-2}) and compelling EE—thanks to the large availability of the reactants at the active sites. However, this approach comes with the disadvantage of significant carbon losses.

It is challenging to achieve, simultaneously, high CE and FE to C-products (CE*FE). One cause of low CE is carbonate formation in the electrolyte and crossover through the membrane; another is the competing hydrogen evolution reaction (HER). It is challenging to achieve, simultaneously, high CE and FE to C-products (CE*FE)

Please cite this article in press as: Park et al., High carbon efficiency in CO-to-alcohol electroreduction using a CO reservoir, Joule (2023), https://doi.org/10.1016/j.joule.2023.08.001

because the CO concentration near the outlet of such systems is low, leading to the competing HER.[2–8]

Cascade electroreduction of CO_2 to CO followed by CORR offers a route to high CE by addressing carbon losses from carbonate formation.[8,9] Commercial solid oxide electrolyzer cells (SOECs) provide a convenient source of CO.[10] However, previous electrochemical CORR systems suffered low CE and product selectivity leading to $CE^*FE_{alcohols} < 25\%$,[8–10] reducing the net energetic benefit.[3,7–9]

We posited that increasing the CO concentration, through local/nanoscale effects, near the catalytic active sites could preserve FE to C-products. Experimentally, we found that—in reference, catalysts based on Cu alone (Figure 1C)—when we tune operating conditions to achieve CE above 30%, the selectivity to C-products drops, resulting in limited adsorbed CO adjacent to metallic copper active sites.

We sought, therefore, to incorporate Cu-NPs into a microporous CO-capturing matrix to ensure CO availability at the catalytic sites (Figure 1D). We implemented this strategy using porous carbon nanoparticles (C-NPs) having functionalized nitrogen (N) groups, which we call carbon reservoir catalyst (CRC) active layers.[11–14] The C-NPs with pyridinic- and pyrrolic-N groups promote CO adsorption while favoring high CORR selectivity to C_{2+} alcohols at high CE. By controlling the reactant diffusion into the porous C-NPs and varying the ratio of pyridinic and pyrrolic-N atoms, we achieved $CE^*FE_{ethanol} > 47\%$ and $EE_{c2+} = 40\%$ sustained for 85 h of continuous operation.

RESULTS AND DISCUSSION

Electrochemical finite-element studies

Since CO solubility in KOH is much lower than that of CO_2,[11] the availability of CO as a reactant will be limited, especially when higher electrolyte concentrations are used and when high current densities are applied. Such a low reactant concentration is expected to result in increased H_2 evolution, limiting the energy and carbon efficiencies of the electrolyzer. Previous investigations have used finite-element modeling (FEM) to study how electrolyzer properties affect performance.[15–22] FEM enables the estimation of local species concentrations.

We explored the distribution of CO in different gas-diffusion electrode (GDE) architectures (Figures 1E–1G; Note S4). We studied how the catalyst performance changes as the reactant distribution varies inside the CL under high CE regimes (high reaction rate, 200 mA cm^{-2}, and low CO flow rate, ca. 1.1 standard cubic centimeters [sccm]). To do this, we modulated the CO adsorption (S_{CO}) in the CL, investigating two scenarios. In the first, the CL contains only catalytic Cu-NPs (without appreciable CO adsorption ability, $S^{\circ}_{CO} = 0$, Figure 1F). In the second, we introduced nanoparticles inside the CL with a markedly different CO adsorption value (S_{CO}*, Figure 1G). As S_{CO} increases, the CO concentration in the gas and liquid phases, which wets the catalyst, also increases (Figures 1F, 1G, S1), potentially enabling higher reactant availability at high CE regimes. A higher S_{CO} is expected to sustain large CO conversion at high CE without an appreciable increase in the HER (Figures S2 and S3). Conversely, without the CRC strategy, regions of the CL with limited CO availability result in pronounced HER at high CE conditions (Figures S4 and S5).

Material preparation and characterization

To implement the CRC strategy, we sought CLs having the CO reservoir property. We looked at gas-absorbing materials able to conduct the high current density

[1]Department of Electrical and Computer Engineering, University of Toronto, Toronto, ON, Canada

[2]Dipartimento di Chimica, Università degli Studi di Milano, Via Golgi 19, 20133 Milano, Italy

[3]CNR-Istituto di Scienze e Tecnologie Chimiche "Giulio Natta", Via C. Golgi 19, 20133 Milano, Italy

[4]Department of Mechanical and Industrial Engineering, University of Toronto, Toronto, ON, Canada

[5]These authors contributed equally

[6]Lead contact

*Correspondence: dave.sinton@utoronto.ca (D.S.), ted.sargent@utoronto.ca (E.S.)

https://doi.org/10.1016/j.joule.2023.08.001

Please cite this article in press as: Park et al., High carbon efficiency in CO-to-alcohol electroreduction using a CO reservoir, Joule (2023), https://doi.org/10.1016/j.joule.2023.08.001

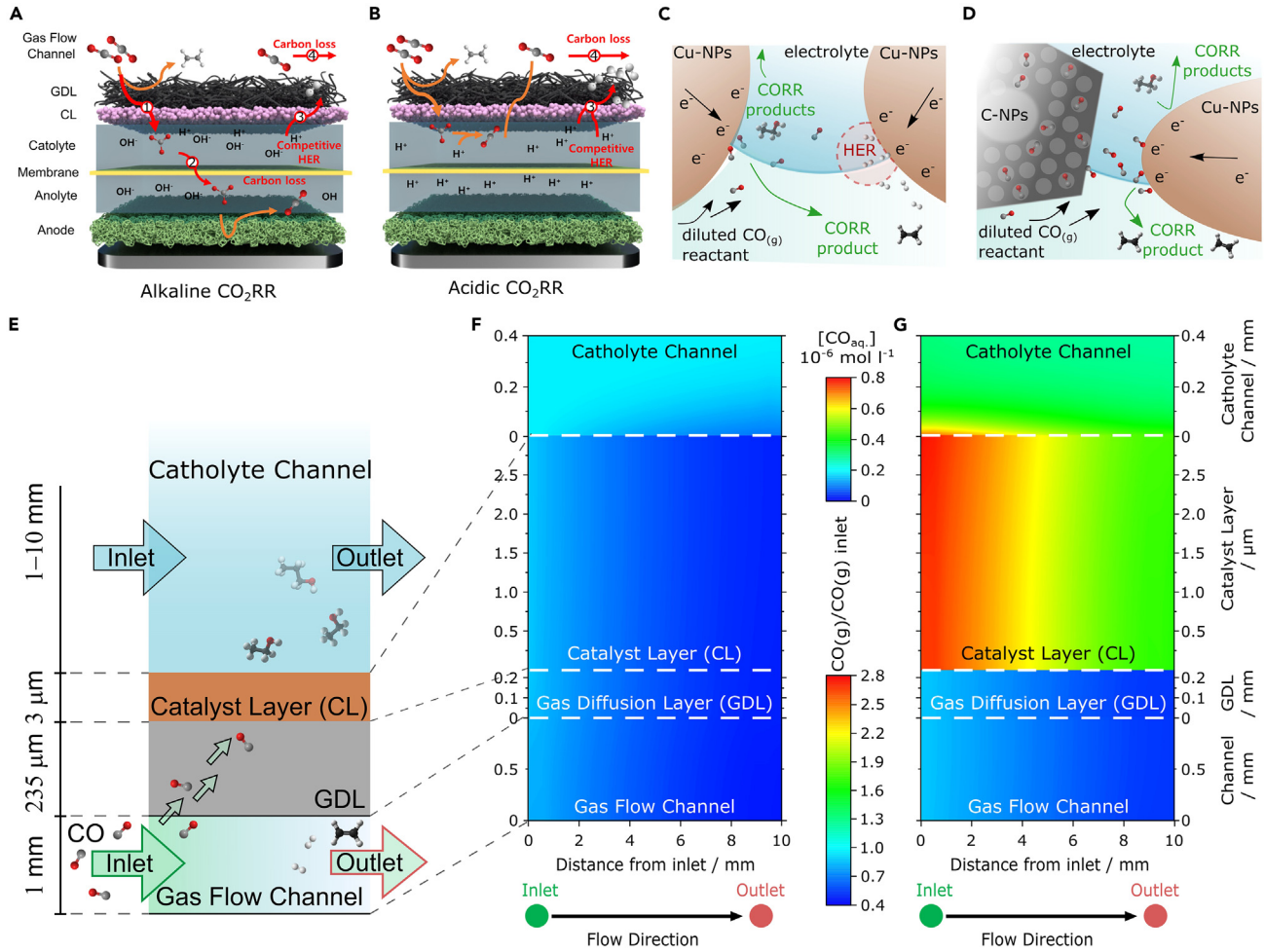

Figure 1. CO availability in the gas phase electrolyzer

(A and B) CO_2RR in (A) basic and neutral media using anion exchange membrane, (B) acidic media using cation exchange membrane. CE losses arise from carbonate formation (1), crossover to the anode side (2) unreacted CO (3). Competition with the hydrogen evolution reaction (4) leads to FE losses.

(C) Catalyst regions where the reactant gas is sparse promote by-product reactions such as HER.

(D) When CO distribution is promoted at the catalytic active sites, CORR to desired C-products can occur at diluted CO conditions.

(E–G) (E) Schematic of the electrolyzer gas cell: the electrolyzer is fed with CO from the gas flow channel inlet. The CO passes through the 10 mm long channel (thickness = 1 mm) and moves into the gas diffusion layer (GDL, thickness = 235 µm) and the catalyst layer (CL, thickness = 3 µm) through convection and diffusion. In the CL, a triple-phase boundary region exists between gaseous CO, solid electrode, and liquid electrolyte (from the catholyte channel, thickness > 1 mm). The gas stream at the gas flow channel outlet is depleted in CO and enriched in C-products and H_2. The CO profile is modeled at 200 mA cm^{-2} and an inlet CO flow rate of ca. 1.1 sccm in the catholyte layer, electrolyzer gas flow channel, inside the unreactive GDL, through a standard CL (F) and a CL with increased carbon monoxide adsorption (S_{CO}) ability (G) and in the catholyte channel. The top scale bar is for the CO dissolved in the electrolyte of the catholyte channel and the bottom scale bar is for the gaseous CO in the CL, GDL, and gas flow channel. Regions of the CL where CO concentration is low favor undesired reactions such as HER (Figure S4). The increased S_{CO} in the carbon reservoir catalyst (CRC) layer extends the dissolved CO availability along the electrode length (in the CL and in the catholyte layer), resulting in favored CORR over HER.

required for reaction rates of industrial interest. Activated microporous C-NPs are adsorbents for CO_2 capture and CO separation and have high structural stability, chemical resistance, and electrical conductibility.[11–13] N-functional groups in porous carbon structures tune surface molecular binding and selectivity in gas separation and electrocatalysis.[14,23–27] Pyridinic- and pyrrolic-N located at the edges of carbon structures (Figure 2A) create active sites interacting with reaction intermediates and driving selectivity in electrocatalytic processes.[28,29] We hypothesized that their assembly with Cu-NPs in a heterojunction CL would offer distinct domains whereby

Please cite this article in press as: Park et al., High carbon efficiency in CO-to-alcohol electroreduction using a CO reservoir, Joule (2023), https://doi.org/10.1016/j.joule.2023.08.001

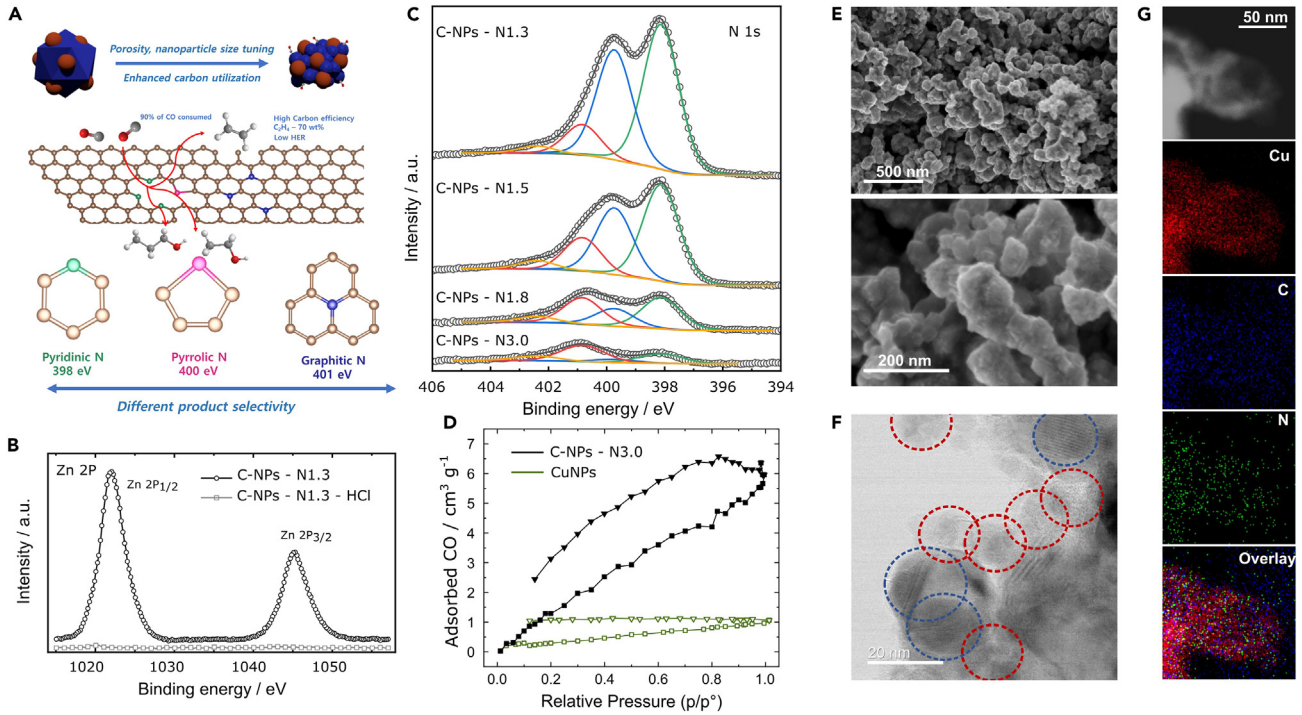

Figure 2. The C-NPs and Cu-NPs CRC heterojunction active layers

(A) Scheme of the different nitrogen groups in N-doped carbon nanoparticles.

(B) Zn 2*p* in the C-NPs with a N_{pi}:N_{pr} ratio of 1:3 before and after acid treatment.

(C) N 1*s* XPS spectra of C-NPs samples with different pyridinic:pyrrolic nitrogen ratios (N_{pi}:N_{pr}) of 1.3, 1.5, 1.8 and 3.0 (in the samples treated at 700°C, 800°C, 900°C, and 1,000°C, respectively).

(D–G) (D) CO adsorption (squares) and desorption (triangles) isotherms for C-NPs with 3.0 N_{pi}:N_{pr} ratio and Cu-NPs (black and green symbols and traces, respectively) (E) SEM, (F) HR-TEM (blue circle—Cu-NPs and red circle—C-NPs N3.0) and (G) HR-TEM with elemental mapping of the three-dimensional (3D) carbon reservoir catalyst (CRC) electrode.

the C-NPs porous structure facilitates CO transport and distribution, and N groups promote selectivity and CO availability.

We used N-rich zeolitic-imidazolate framework (ZIF)-derived carbon as a material to prepare micro-, meso-, and macroporous carbon structures. As the heat-treatment temperature tunes physicochemical and structural properties, we prepared different types of C-NPs under different heat-treatment temperatures of 700°C, 800°C, 900°C, and 1,000°C. Thermal treatment above 700°C removes most methyl groups of the organic framework. Higher temperature leads to the removal of carbon species and N, and the evaporation of the Zn metal species occurs above 900°C. The remaining Zn is removed by acid treatment with concentrated HCl (Figure 2B), resulting in Zn-free C-NPs. Additionally, we controlled the nanoparticle size by adjusting the synthesis temperature, obtaining ~25 and ~100 nm C-NPs at room temperature and 0°C, respectively.

The XPS spectra of the N 1*s* can be deconvolved in four peaks: pyridinic-N (N_{pi}, at 398.0 eV), pyrrolic-N (N_{pr}, at 400 eV), graphitic-N (N_g, at 401 eV), and oxidized-N (N_o, at 403 eV) (Figures 2A and 2C; Table S9).[22,23] Thermal treatment tuned the pyrrolic: pyridinic-N atom ratio (N_{pi}:N_{pr}) from ca. 1.3 to 3.0 in the C-NPs treated at 700°C and 1,000°C (denoted as C-NPs-N1.3 and C-NPs-N3.0, respectively) without change in the morphology of the nanoparticles (Figures 2E–2G and S13–S16). Cyclic CO adsorption and desorption experiments reveal that the C-NPs, regardless of the

N_{pi}:N_{pr} ratio, have a 6–9 cm^3 g^{-1} CO adsorption capacity (S_{CO}), which is reversible (Figures 2D and S9).

The linear adsorption profile indicates relatively weak adsorbent-adsorbate interactions.[30] At each relative pressure, CO molecules cluster around the most favorable sites in the C-NPs samples. The hysteresis in the complete loop confirms that the pores are partially filled with CO. These features in the adsorption-desorption cycle and the similar CO adsorption values at each N content and N_{pi}:N_{pr} ratio are consistent with physisorption behavior.[10,13]

Conversely, Cu-NPs have a low 1 cm^3 g^{-1} S_{CO} in the adsorption cycle linked to the presence of Cu^{2+} and Cu^{1+} oxidized Cu sites (Figure 2D) at the surface due to the passivation of these commercial nanoparticles. The negligible CO desorption implies that Cu-NPs irreversibly chemisorb CO at room temperature.[24] These results suggest that C-NPs may capture and release CO under CORR conditions and increase the CO availability of nearby catalytic Cu-NPs.

We assembled CRC GDEs with catalytic Cu-NPs, C-NPs, and Nafion ionomer to extend ion and CO diffusivity. Scanning electron microscopy (SEM, Figures 2E, S11–S16, and S23 for the 100 nm C-NPs) shows that C-NPs and Cu-NPs aggregate in ca. 200 nm structures bound with Nafion. High-resolution transmission electron microscopy (Figure 2F) further indicates that C-NPs and Cu-NPs are homogeneously mixed in these structures. Elemental energy dispersive X-ray spectroscopy of a CRC with C-NPs-N1.3 (CRC_N1.3, Figures 2G and S10–S17 for CRC_N3.0) also confirms the presence of a continuous Cu and C-NPs network only with a few C-NPs agglomerates.

CO electroreduction performance in flow cells

Flow cells with a GDE were used to study electrocatalytic performance at operating current densities > 100 mA cm^{-2} to explore ethanol FE and CE. The C-NPs with different sizes and N_{pi}:N_{pr} were implemented into CRC active layers and tested at 100, 200, 300, and 400 mA cm^{-2} (Figure S18) using 4 M KOH and anion exchange membrane (AEM). At 200 mA cm^{-2}, CRC electrodes show enhanced selectivity to alcohols (ethanol and propanol) compared with pure Cu-NPs ($FE_{C2+\ alcohols}$ ~ 48% vs. 32%, respectively).

Alcohol FE increases at the expense of ethylene and hydrogen in the CRC system compared with relevant Cu-NP controls (Figure 3A). Tuning the ratio of pyridinic:pyrrolic-N atoms shifts the alcohol selectivity. The CRC with N_{pi}:N_{pr} 1.3 synthesized at 700°C, provides the highest propanol productivity, 32% FE, at 200 mA cm^{-2}. The nucleophilicity of pyridinic-N may facilitate *OCCO and *CO bonding, a route to increase propanol at the expense of ethanol.[25–27] A larger ratio of pyrrolic vs. pyridinic-N within CRC-N3.0 inhibits C_{3+} alcohol formation, leading to the highest ethanol FE, 30% FE, at 200 mA cm^{-2} while maintaining total alcohol FE (ethanol selectivity over total alcohol increases from 38% to 63% as the amount of pyrrolic-N increases).[25]

We then further explored the ratio of Cu-NPs and C-NPs-N3.0 (CRC-N3.0) to maximize CE by acting on the CO flow rate (from 0.5 to 10 sccm, Figures 3B and 3C). Detailed experimental data on gas flow rate, CE, and FE are described in the supplemental information (Table S11). Different catalyst loading, C-NPs: Cu-NPs ratios, and ionomer loading ratios were also performed to optimize FE and CE (Figures S20 and S21).

Please cite this article in press as: Park et al., High carbon efficiency in CO-to-alcohol electroreduction using a CO reservoir, Joule (2023), https://doi.org/10.1016/j.joule.2023.08.001

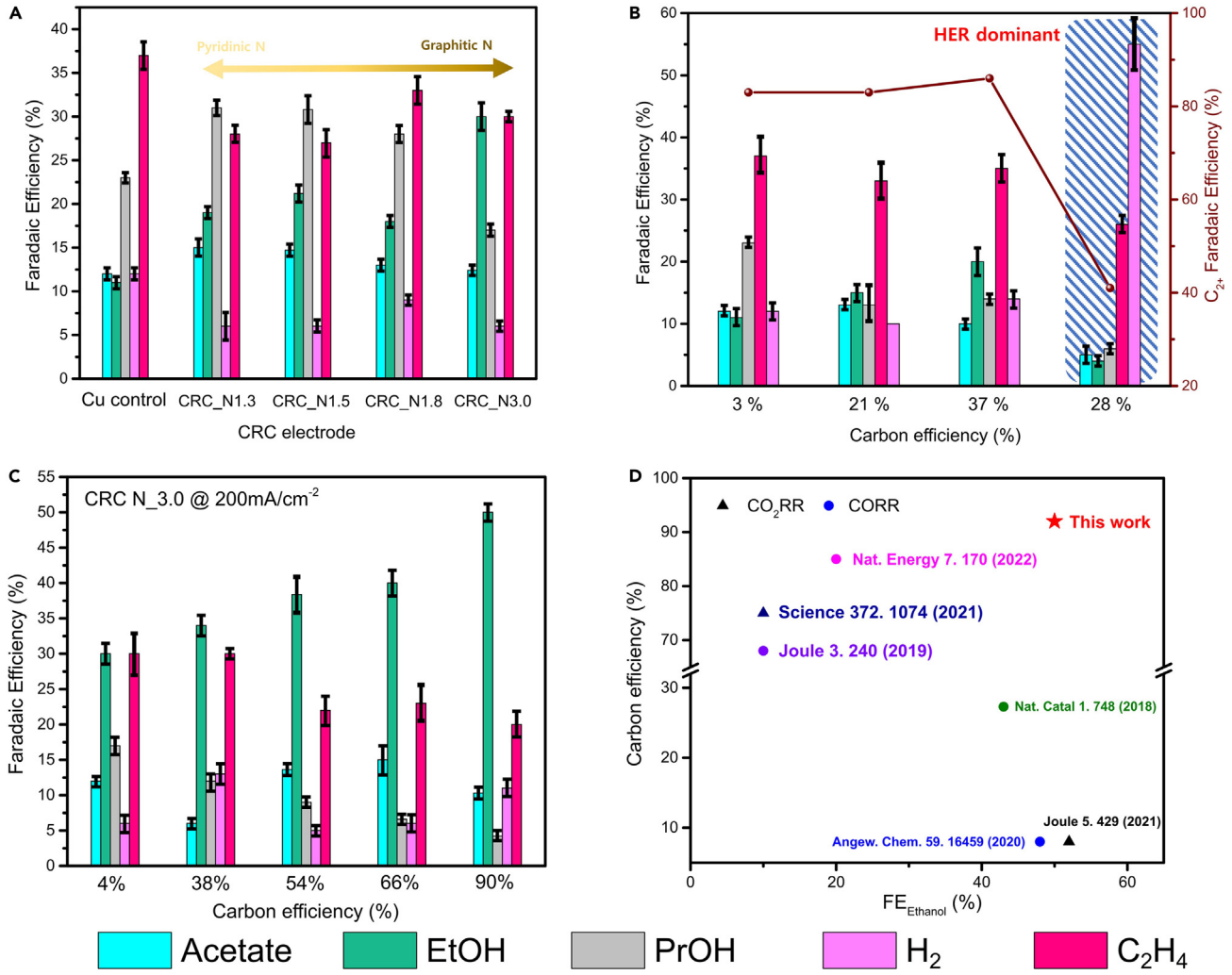

Figure 3. Heterojunction carbon reservoir catalysts for carbon-efficient CO electroreduction to alcohols

(A–C) (A) Comparison of product distribution at 200 mA cm^{-2} and 20 sccm of CO on different CRC GDEs comprising C-NPs with different N_{pi}:N_{pr} ratios and catalytic Cu-NPs catalysts. FE distribution of CORR products at 200 mA cm^{-2} for (B) control Cu-NPs and (C) CRC_N3.0 tested at different CE and CO flow (detailed information in the Tables S6 and S7).

(D) Plot of FE ethanol versus external carbon efficiency for various catalysts in CO_2RR/CORR (detailed information in the Table S8).

A GDE containing only Cu-NPs achieved 32% CE and 20% FE of EtOH ($CE*FE_{ethanol}$ = 6%) and overall, 84% FE to C_{2+} (Figure 3B). In this case, ethylene was the dominant product, and HER steeply increased at CE above 30%, suggesting that the local concentration of CO decreased, disfavoring CO–CO coupling to C_{2+} products, and limiting CE.

CRC electrodes extend C_{2+} production above 30% CE. We tested the two C-NPs sizes (25 and 100 nm) and found that, with 100 nm C-NPs, HER takes over even in CO rich environment (Figures S22 and S23). We then characterized in detail the pore size distribution and structure of the C-NPs using N_2 adsorption-desorption isotherms and pore size distribution analysis. All the C-NPs samples have a high specific surface area (from Brunauer-Emmett-Teller [BET], Figure S7). Both C-NPs show similar micropores and mesopores (below 1 nm and ca. 2–3 nm diameter, respectively) distributions. However, the 100 nm C-NPs present larger macropores (with

a diameter of 70–90 nm compared with 20–30 nm for the smaller C-NPs). Macroporous structures are due to the interparticle voids and promote kinetic accessibility to the available active sites favoring mass- and ionic transport.[28,29,31] In 100-nm C-NPs heterojunction CRC electrodes, Cu-NPs could segregate in the large macropores with limited CO distribution, causing HER (Figure S23).

CRC electrodes assembled with 25 nm C-NPs achieve CE and C_{2+} production above 90% (Table S10). We optimized the CRC-N3.0 electrode and achieved 50% FE to EtOH and CE 90% ($CE^*FE_{ethanol}$ = 47%) with, overall, 93% FE to C_{2+} (Figure 3C), outperforming previous reports, especially in terms of simultaneous achievement of CE and ethanol FE (Figure 3D; Table S12). Moreover, ethanol selectivity over total alcohol increases from 63% to 90% at a low CE of 12% CE to 90% CE, respectively. The CRC catalyst functions as a CO reservoir that can modulate the local concentration of CO even in a low CO supply. The modulation of CO local concentration would suppress deoxygenation of HOCCH* that favors the formation of alcohol and maintains high C_{2+} FE at low CO supply.[25,32,33]

In situ characterization

To analyze the oxidation state of the catalyst under CORR conditions, we performed X-ray absorption spectroscopy (XAS) at the Cu K-edge of control samples (Cu_2O, CuO, and Cu metal), Cu-NPs, and the CRC-N3.0 electrodes as prepared, and during CORR (EXAFS in Figure 4A). Before the reaction, the Cu nanoparticles are partially oxidized at the surface with oxidation number +1. In *operando* conditions, the EXAFS spectrum of CRC shows that the copper oxide shell becomes fully reduced, suggesting an active catalyst composed of Cu metal.

We used *in situ* and *operando* Raman spectroscopy to query the reaction in different catalyst architectures—Cu-NPs, CRC-N1.3, and CRC-N3.0) during CORR (Figure 4B). The signal intensity under −0.25 V_{RHE} (which corresponds to a low current density, ca. 5 mA cm^{-2}) we took to be a qualitative indicator of the CO* saturation coverage.[34] Under this potential, the bands at 280 and 360 cm^{-1} associated with a frustrated rotation and stretching of *CO on the Cu, respectively, show a shift to lower frequencies in the CRC catalysts. This shift implies a weaker Cu–CO bond that suggests partial coordination of the adsorbed CO with the N-functional groups of the C-NPs.[35,36] As the applied potential stepped to more negative values, the peaks shifted to higher frequencies indicating the prevalence of the stronger Cu–CO bond at high reaction rates.

The band in the range of 1,900–2,100 cm^{-1} arises from the C≡O stretching atop bound, which is an on-pathway intermediate to C_{2+}.[37] The peak is present at the surface of CRC electrodes at more negative voltages than Cu-NPs. These voltages correspond to reaction rates at which CO is depleted in the reactant gas and are compatible with CO-diluted conditions occurring at high CE^*FE_{C2+}. Additionally, the broad peak on CRC electrodes indicates that the presence of the many different N groups of C-NPs modulates the CO binding sites and leads to high alcohol selectivity.[38] In CRC electrodes, the catalytic sites are present only at the surface of Cu-NPs that are surrounded by C-NPs (Figures 2E–2G and S17). Prior studies showed that surface Cu^{2+} binds pyridinic and pyrrolic N[39,40] in catalytic materials and suggests that in the CRC electrode, C-NPs can coordinate with the partially oxidized Cu-NPs (Figure S8). *Operando*, the heterojunction structure can provide confined spaces where catalytic Cu surface sites and N groups are within distances to bind reaction intermediates and affect the selectivity.

Please cite this article in press as: Park et al., High carbon efficiency in CO-to-alcohol electroreduction using a CO reservoir, Joule (2023), https://doi.org/10.1016/j.joule.2023.08.001

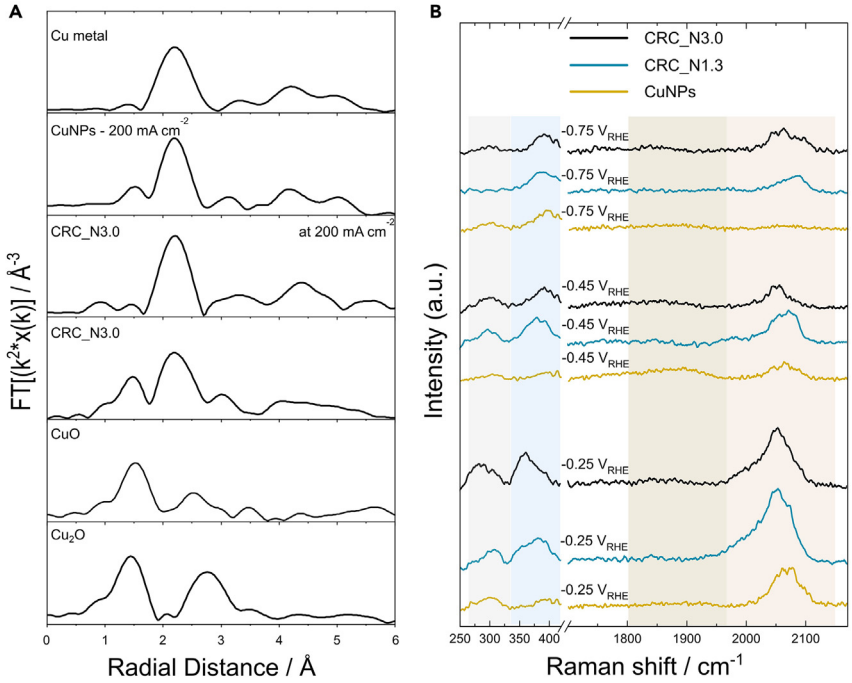

Figure 4. *Operando* characterization of carbon reservoir catalyst electrodes

(A) Cu K-edge EXAFS spectra of Cu_2O, CuO, and Cu metal reference materials, a C-NPs/Cu-NPs electrode (CRC_N3.0) *ex situ* and CRC_N3.0 and Cu-NPs electrode under CORR *operando* condition at 200 mA cm^{-2}.

(B) *Operando* Raman spectra of Cu-NPs, CRC_N1.3, and CRC_N3.0 (yellow, blue, and black traces, respectively) electrodes under CORR at different applied potentials. The region of 250–325 cm^{-1} (*CO frustrated rotation), 325–425 cm^{-1} (*CO stretching), 1,850–2,000 cm^{-1} (stretching of bridge bound *CO), and 2,000–2,150 cm^{-1} (stretching of atop-bound *CO) are marked by gray, blue, brown, and orange, respectively. The Raman shift between 425 and 1,700 cm^{-1} is marked by the break in the x axis.

Taken together, *operando* XAS and Raman show that C-NPs influence the CO adsorption on the active catalytic sites of metallic copper and correlate the enhanced CE and FE to C_{2+} alcohols to the extended availability of CO and the multitude of binding sites in the CRC catalysts.

Membrane electrode assembly for stability testing

We implemented the CRC in membrane electrode assembly (MEA) system, allowing longer operating times and low resistive losses.[7] We achieved a full-cell voltage of −2.35 V at a current density of 100 mA cm^{-1} using 2 M KOH as anolyte and observed stable operation for over 85 h (Figure 5A). This corresponds to a full-cell C_{2+} EE of 39% and alcohol EE of 24%. We carried out techno-economic (Note S1) and carbon footprint analyses using experimental data from the CORR MEA system (Note S2).[37,41]

We estimated the plant-gate levelized cost per ton of ethanol assuming CO_2RR to CO via SOEC and CORR as studied herein (details in Note S1). In the MEA configuration, the total plant-gate levelized cost (including estimated separation costs) per ton of ethanol is less than the sum of hydrogen, ethylene, propanol, and ethanol product values (Figure 5B). The energy cost of CO_2RR and CORR is ~200 GJ $tonne^{-1}_{EtOH}$ (Figure 5B; Table S2). With 83% CE, the CORR system based on the optimized catalyst has (cradle-to-gate) projected at -1.1 $tonne_{CO_2}/tonne_{EtOH}$ (Note S1).

Please cite this article in press as: Park et al., High carbon efficiency in CO-to-alcohol electroreduction using a CO reservoir, Joule (2023), https://doi.org/10.1016/j.joule.2023.08.001

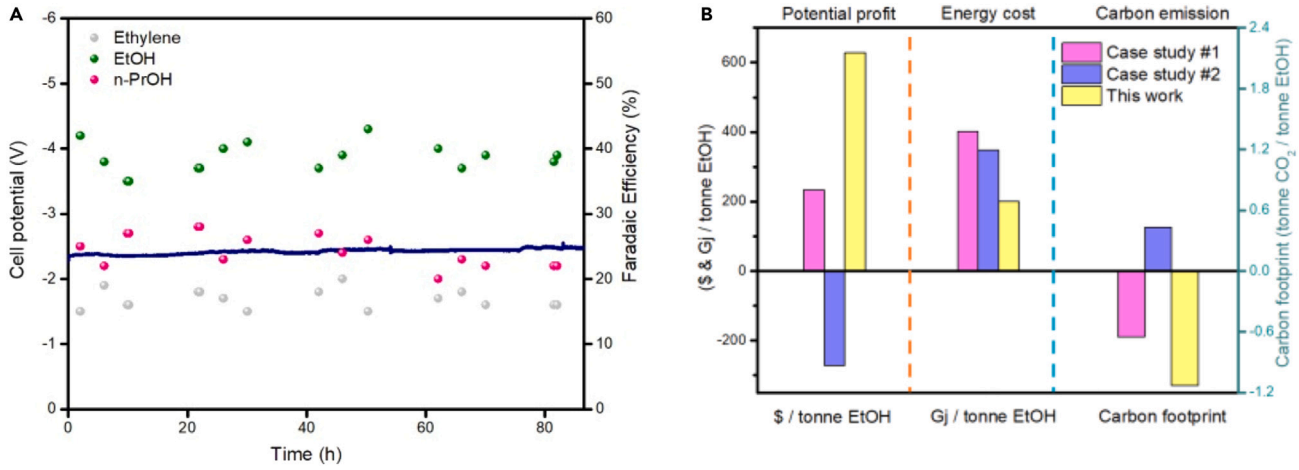

Figure 5. Techno-economic and carbon footprint analysis comparison for different case studies and stability test

(A) Chronopotentiometry stability test of CRC_N3.0 at 100 mA cm^{-2} in MEA cell configuration.

(B) TEA and carbon footprint analysis and comparison with different case studies (detailed information in the Notes S1–S3).[2,32]

Conclusion

The CRC provides catalysts that are not limited by CO depletion near the outlet of an electrolysis system, enabling alcohol selectivity to be maintained at high CE. The choice of N in the CRC increases the selectivity toward ethanol (50% ± 3%) against propanol in flow cell system, driven by pyridinic vs. pyrrolic-N. In an MEA, the catalyst performed >85 h of electrosynthesis at 100 mA cm^{-2}, with a CE of 83%, 40% ethanol FE, and 40% EE_{C2+}. With energy analysis over the cascade system, the performance of the CRC catalyst suggests the CORR-to-ethanol has a path to carbon-negative ethanol electrosynthesis, paving the way to the decarbonization of the chemical industry.

EXPERIMENTAL PROCEDURES

Resource availability

Lead contact

Further information and requests for resources and materials should be directed to and will be fulfilled by the lead contact, Edward H. Sargent (ted.sargent@utoronto.ca).

Materials availability

Further information and requests for resources and materials should be directed to and will be fulfilled by the lead contact, Edward H. Sargent (ted.sargent@utoronto.ca).

Data and code availability

The original data supporting the current study are available from the lead contact on request.

Preparation of catalyst and gas-diffusion electrode

Materials

2-Methylimidazole 99%, Zn $(NO_3)_2$ ethanol, HCl (37 wt %), KOH, dimethyl sulfoxide (DMSO), deuterated water (D_2O), and methanol were used as purchased from Aldrich. Carbon monoxide (grade 4) was purchased from Praxair, and Ar (grade 5) was purchased from Messer. Nickel foam was purchased from MTI Corporation.

Please cite this article in press as: Park et al., High carbon efficiency in CO-to-alcohol electroreduction using a CO reservoir, Joule (2023), https://doi.org/10.1016/j.joule.2023.08.001

Carbon-based GDE (Freudenberg H23C9), AEM (Fumasep FAA-PK-130), Nafion 212, 5% Nafion perfluorinated resin solution 5 wt % (D520 EW = 1,000) were purchased from the Fuel Cell Store. Deionized water (18.2 MΩ) was used in all experiments.

Synthesis of electrocatalysts

Synthesis of the 25 nm ZIF (25-ZIF): at room temperature, add a solution of 500 mL of methanol containing 2-methylimidazole (13.57 g) to a solution of 500 mL of methanol containing $Zn(NO_3)_2$ (12.29 g) under stirring. After a few minutes, the solution turns white, and after 20 min, stop the stirring and leave the solution settling for 24 h at room temperature. Then, decant the supernatant clear solution, separate the white precipitate by centrifugation, wash it with methanol three times, and finally dry it overnight under a vacuum.

Synthesis of the 200 nm ZIF (200-ZIF): dissolve 2-methylimidazole (3.24 g) in 175 mL of methanol and dissolve $Zn(NO_3)_2$ (2.94 g) in 175 mL of methanol. After cooling the two solutions in an ice bath, add the methylimidazole solution to the Zn solution under stirring at 300 rpm. Stir for 2 min, remove from the stirrer, and leave settling undisturbed for 24 h at room temperature. Then, decant the supernatant clear solution, separate the white precipitate by centrifugation, wash with methanol three times, and finally dry it overnight under vacuum.

Thermal treatment: we used a thermal treatment to remove the Zn from the organic structure and obtain the C-NPs powder. White ZIF powder (500 mg) was placed in a quartz boat and annealed in a tube furnace under an inert atmosphere by flowing Ar at 100 cm^3 min^{-1}. The final temperature was reached with a two-ramp process. Initially, the powder was heated at a rate of 5°C min^{-1} up to 650°C and left at this temperature for 1 h. Then, the temperature was increased at a rate of 5°C min^{-1} to the final annealing temperature (700°C, 800°C, 900°C, and 1,000°C), which was maintained for 2 h. During the annealing process, the weight loss was ca. 50%, 40%, 35%, and 30% for the samples treated at 700°C, 800°C, 900°C, and 1,000°C, respectively.

Acid treatment: we treated the obtained C-NPs powder with concentrated HCl to remove the residual Zn. C-NPs (100 mg) were stirred with 10 mL of concentrated HCl for 24–72 h. Then, the powder was separated by centrifugation, washed with deionized water four times, and finally with ethanol.

Preparation of gas-diffusion electrode

The catalyst was airbrushed on a Freudenberg H23C9 (Fuel Cell Store) GDE with dimensions of 3 × 3 cm^2 or 2 × 2 cm^{-2}. The ink was prepared by adding Cu-NPs and the NDC to 2 mL of propanol. After a few seconds of sonication, a 5% Nafion solution (Fuel Cell Store D520, EW = 1,000) was added. A typical ink contained 80 μL of Nafion, 20 mg Cu-NPs, and 2 mg of NDC. The ink was sonicated for more than 1 h before being deposited on the GDE.

Adsorption measurements

Gas sorption measures were performed with a Micromeritics 3Flex instrument. The specific surface areas were determined from the N_2 desorption isotherm at 77 K in the pressure range between 0.05 and 0.3 (relative pressure, p/p°), according to the BET method. CO sorption studies were carried out at room temperature and up to 1 bar. Before N_2 and CO adsorption analyses, the samples were thermally treated at 393 K for 12 h under high vacuum (10^{-6} Torr).

Please cite this article in press as: Park et al., High carbon efficiency in CO-to-alcohol electroreduction using a CO reservoir, Joule (2023), https://doi.org/10.1016/j.joule.2023.08.001

Structural characterization

The TEM imaging was conducted on a JEOL EM-2010 microscope operated at 200 kV. STEM imaging and EDS measurements were performed in STEM mode equipped with a single drift detector (X-MAX^N Oxford Instruments). SEM imaging was conducted on a Hitachi FE-SEM SU5000 microscope operated at 30 kV. The powder samples were deposited on a carbon tape before SEM imaging. XRD analysis was performed on a MiniFlex600 system employing Cu Kα radiation. XPS measurements were conducted using the PerkinElmer model 5600, equipped with 1,486.6 eV monochromated Al Kα X-ray source. The samples were prepared on conductive glass substrates by drop-casting a few droplets of ink solution.

Electrochemical CO reduction measurements

Electrochemical rate measurements were performed in both a flow cell and a MEA configuration. For the flow cell setup, the catalyst-deposited GDE was used as the working electrode (cathode) and nickel foam (MTI Corporation) as the counter electrode (anode). An AEM (Fumasep FAA-PK-130) was used to separate the anodic and cathodic compartments. The flow cell assembly constituted of the GDE, AEM, and nickel anode, whereas liquid electrolyte (4 M KOH, Sigma Aldrich) was circulated in both anodic and cathodic compartments using a peristaltic pump (McMaster-Carr). Carbon monoxide (Praxair, Grade 4.0) was passed behind the GDE using a mass flow controller (Sierra SmartTrack 100), while an Ag/AgCl reference electrode was inserted inside the cathodic compartment for half-cell potential measurement. For the MEA setup, the catalyst-deposited GDE was used as the working electrode (cathode), and an IrO_2-Ti felt (Sigma Aldrich) as the anode. A Nafion 212 (Fuel Cell Store) cation-exchange membrane was used to keep separation between the anolyte and the cathodic liquid products. The MEA was assembled by layering the GDE, Nafion, and IrO_2-Ti felt and pressing them between the cathode plate (1 cm^2 flow field, stainless steel) and the anode plate (5 cm^2 titanium, flow field). A 1 M KOH solution was circulated through the anodic flow field using a peristaltic pump, whereas carbon monoxide was flown into the cathodic flow field using a mass flow controller. The liquid products were collected inside a cooled container (2°C–6°C) from the outlet of the cathode plate. For both configurations, the carbon monoxide flowrate was 25–40 sccm, and the electrolyte flow was 10–15 mL min^{-1}. Electrochemical reactions were performed using an electrochemical workstation (Autolab PGSTAT302N) connected to a current booster (Metrohm Autolab, 10 A). Electrode potentials were rescaled to the RHE reference by:

$$E_{Vs\ RHE} = E_{Vs\ Ag/AgCl} + 0.235V + 0.059 \times pH$$

An electrochemical impedance spectroscopy (EIS) measurement using an Autolab PGSTAT302N electrochemical workstation was performed to obtain a cell resistance of 3.51 Ω. iR corrections to the potential were then performed using the following equation:

$$E_{iR-free} = E_{Vs\ Ag/AgCl} - 0.85 R_{cell} i_{cell}$$

where $E_{iR\text{-}free}$ is the corrected potential at the cathode, $E_{Vs\ Ag/AgCl}$ is the applied potential, and i_{cell} is the total current (a negative value at the cathode). A correction factor of 0.85 is used due to the 1 M KOH electrolyte's high conductance and low voltage drop across the electrolyte.

The full-cell EE of the MEA system is obtained from the following equation:

$$EE_{Full-cell} = FE_{Product} \times \frac{E^0_{cell}}{V_{Full-cell}}$$

where $EE_{Full\text{-}cell}$ is the full-cell EE of the system, $FE_{Product}$ is the system's FE toward specific product, and $V_{Full\text{-}cell}$ is the average full-cell voltage over the length of the stability experiment. The standard reduction potential of the cell is obtained from the standard Gibbs free energy of the reaction $2CO + 3H_2O \rightarrow CH_3CH_2OH + 2O_2$:

$$E^0_{cell} = \frac{-\Delta G^0_{2CO+3H2O \rightarrow Ethanol+2O2}}{zF}$$

where z is equal to 8 and F is the Faraday constant (96,485 C mol^{-1}).

Product analysis

The gas products from CORR were analyzed by sampling 1 mL of the electrolyzer outlet gas with an air-tight syringe (Hamilton, 5 mL). The gas sample was injected into a gas chromatograph (Shimadzu GC-2014) equipped with a thermal conductivity detector (TCD) and a flame ionization detector (FID). A Molecular Sieve 5A and Carboxen-1000 column were installed upstream of the TCD and FID, respectively, to separate the H_2, CO and gaseous hydrocarbons. The liquid products were quantified using nuclear magnetic resonance (NMR) spectroscopy (Figure S24 shows representative analyses of the liquid products). A 1 mL sample of the electrolyte was taken at various times during the reaction. 1H NMR spectra of the analyte samples were taken using an Agilent DD2 600 spectrometer with DMSO as an internal standard. FE of CORR gas product was calculated by the following equation:

$$FE_{i,gas} = y_{i,g}\dot{V}z_iF\frac{P_0}{RT}j_{total}$$

where y_i is the volume fraction of gas product i, V is the outlet gas flow rate in sccm, z_i is the number of electrons associated with producing one molecule of i, F is the Faraday constant, P_0 is atmospheric pressure, R is the ideal gas constant, T is the temperature, and j_{total} is the total current density. The FE of liquid product was calculated using the following equation:

$$FE_{i,liquid} = n_{i,liquid}z_iF\frac{1}{Q_{total}}$$

where n_i is the number of moles of liquid product i, and Q is the total charge passed prior to the liquid sample being taken.

Operando and *ex situ* spectroscopic analysis

We carried out *operando* and *ex situ* XAS Cu K-edge measurements at the European Synchrotron Radiation Facility (ESRF) at beamline ID26 which is equipped with high energy resolution fluorescence detectors (HERFDs). We employed a flow cell electrolyzer modified to host a X-ray transparent window facing the cathode backside.

Operando Raman was operated with a water immersion objective with a Renishaw inVia Raman microscope using a 785 nm laser. To avoid damaging the samples, we collected full spectrum in two ranges (centered at 700 and 1,700 cm^{-1}) using 0.05% full laser intensity, 0.1 s integration time, and 200 repetitions. The raw data were base corrected by using Origin 2019 software. An open-structured flow cell was utilized for the measurements. An Ag/AgCl electrode (with saturated aqueous KCl solution) and a platinum wire were the reference and counter electrode, respectively. We collected the spectra at different current densities per each CL.

SUPPLEMENTAL INFORMATION

Supplemental information can be found online at https://doi.org/10.1016/j.joule.2023.08.001.

ACKNOWLEDGMENTS

This work was supported by the Natural Sciences and Engineering Research Council (NSERC) of Canada (number RGPIN-2017-06477, E. Sargent) and the Ontario Research Fund—Research Excellence Program (number ORF-RE08-034, E. Sargent). D.S. acknowledges the NSERC E.W.R. Steacie Memorial Fellowship. T.A. acknowledges funding through an NSERC scholarship. I.G. acknowledges the European Union's Horizon 2020 research and innovation program under Marie Sklodowska-Curie grant (agreement no 846107). This research used resources of the European Synchrotron Radiation Facility (ESRF) at beamline ID26 during the experimental session MA5352 (https://doi.org/10.15151/ESRF-ES-744180074). We thank R. Wolowiec and D. Kopilovic for their kind technical assistance, Ontario Centre for the Characterization of Advanced Materials (OCCAM) of the University of Toronto, and the National Synchrotron Radiation Research Center.

AUTHOR CONTRIBUTIONS

E. Sargent supervised the project. S.P., I.G., and E. Sargent conceived the idea. S.P. and I.G synthesized catalyst, carried out the experiments, and performed characterization. F.B. and J.K. performed N_2 and CO adsorption and desorption experiments. I.G. and T.A. performed theoretical calculations. B.-H.L., E. Shirzadi, R.D., G.L., Y.L., A.S.Z., D.S., and D.K. contributed to the manuscript editing. S.P., I.G., T.A., and E. Sargent co-wrote the manuscript. J.A performed *in situ* XAS measurements. B.-H.L., J.K., E.D.J., and D.K. assisted with the discussions.

DECLARATION OF INTERESTS

The authors declare no competing interests.

Received: February 21, 2023
Revised: June 30, 2023
Accepted: August 2, 2023
Published: August 25, 2023

REFERENCES

1. Jouny, M., Luc, W., and Jiao, F. (2018). General techno-economic analysis of CO_2 electrolysis systems. Ind. Eng. Chem. Res. *57*, 2165–2177.
2. Huang, J.E., Li, F., Ozden, A., Sedighian Rasouli, A., García de Arquer, F.P., Liu, S., Zhang, S., Luo, M., Wang, X., Lum, Y., et al. (2021). CO_2 electrolysis to multicarbon products in strong acid. Science *372*, 1074–1078.
3. O'Brien, C.P., Miao, R.K., Liu, S.J., Xu, Y., Lee, G., Robb, A., Huang, J.E., Xie, K., Bertens, K., Gabardo, C.M., et al. (2021). Single pass CO_2 conversion exceeding 85% in the electrosynthesis of multicarbon products via local CO_2 regeneration. ACS Energy Lett. *6*, 2952–2959.
4. Yan, Z.F., Hitt, J.L., Zeng, Z.C., Hickner, M.A., and Mallouk, T.E. (2021). Improving the efficiency of CO_2 electrolysis by using a bipolar membrane with a weak-acid cation exchange layer. Nat. Chem. *13*, 33–40.
5. Ripatti, D.S., Veltman, T.R., and Kanan, M.W. (2019). Carbon monoxide gas diffusion electrolysis that produces concentrated C2 products with high single-pass conversion. Joule *3*, 240–256.
6. Xie, Y., Ou, P.F., Wang, X., Xu, Z.Y., Li, Y.C., Wang, Z.Y., Huang, J.E., Wicks, J., McCallum, C., Wang, N., et al. (2022). High carbon utilization in CO_2 reduction to multi-carbon products in acidic media. Nat. Catal. *5*, 564–570.
7. Xu, Y., Miao, R.K., Edwards, J.P., Liu, S.J., O'Brien, C.P., Gabardo, C.M., Fan, M.Y., Huang, J.E., Robb, A., Sargent, E.H., et al. (2022). A microchanneled solid electrolyte for carbon-efficient CO_2 electrolysis. Joule *6*, 1333–1343.
8. Ozden, A., Wang, Y.H., Li, F.W., Luo, M.C., Sisler, J., Thevenon, A., Rosas-Hernández, A., Burdyny, T., Lum, Y.W., Yadegari, H., et al. (2021). $_2$ electroreduction enables efficient carbonate-free production of ethylene. Joule *5*, 706–719. Cascade.
9. Ozden, A., Li, J., Kandambeth, S., Li, X.-Y., Liu, S., Shekhah, O., Ou, P., Zou Finfrock, Y., Wang, Y.-K., Alkayyali, T., et al. (2023). Energy- and carbon-efficient CO_2/CO electrolysis to multicarbon products via asymmetric ion migration–adsorption. Nat. Energy *8*, 179–190.
10. Jouny, M., Hutchings, G.S., and Jiao, F. (2019). Carbon monoxide electroreduction as an emerging platform for carbon utilization. Nat. Catal. *2*, 1062–1070.
11. Gadipelli, S., and Guo, Z.X. (2015). Tuning of zif-derived carbon with high activity, nitrogen functionality, and yield - a case for superior CO_2 capture. ChemSusChem *8*, 2123–2132.
12. Ding, M.L., Flaig, R.W., Jiang, H.L., and Yaghi, O.M. (2019). Carbon capture and conversion using metal-organic frameworks and mof-based materials. Chem. Soc. Rev. *48*, 2783–2828.
13. Geng, Z., Xiao, Q.F., Lv, H., Li, B., Wu, H.B., Lu, Y.F., and Zhang, C.M. (2016). One-step synthesis of microporous carbon monoliths derived from biomass with high nitrogen doping content for highly selective CO_2 capture. Sci. Rep. *6*, 30049.
14. Babarao, R., Dai, S., and Jiang, D.E. (2012). Nitrogen-doped mesoporous carbon for carbon capture - a molecular simulation study. J. Phys. Chem. C *116*, 7106–7110.
15. García de Arquer, F.P.G., Dinh, C.T., Ozden, A., Wicks, J., McCallum, C., Kirmani, A.R., Nam, D.H., Gabardo, C., Seifitokaldani, A., Wang, X., et al. (2020). CO_2 electrolysis to multicarbon

products at activities greater than 1 A/cm^{-2}. Science *367*, 661–666.

16. Kas, R., Star, A.G., Yang, K.L., Van Cleve, T., Neyerlin, K.C., and Smith, W.A. (2021). Along the channel gradients impact on the spatioactivity of gas diffusion electrodes at high conversions during CO_2 electroreduction. ACS Sustainable Chem. Eng. *9*, 1286–1296.

17. Weng, L.C., Bell, A.T., and Weber, A.Z. (2020). A systematic analysis of cu-based membrane-electrode assemblies for CO_2 reduction through multiphysics simulation. Energy Environ. Sci. *13*, 3592–3606.

18. Weng, L.C., Bell, A.T., and Weber, A.Z. (2018). Modeling gas-diffusion electrodes for CO_2 reduction. Phys. Chem. Chem. Phys. *20*, 16973–16984.

19. Kas, R., Yang, K.L., Yewale, G.P., Crow, A., Burdyny, T., and Smith, W.A. (2022). Modeling the local environment within porous electrode during electrochemical reduction of bicarbonate. Ind. Eng. Chem. Res. *61*, 10461–10473.

20. Hashiba, H., Weng, L.C., Chen, Y.K., Sato, H.K., Yotsuhashi, S., Xiang, C.X., and Weber, A.Z. (2018). Effects of electrolyte buffer capacity on surface reactant species and the reaction rate of CO_2 in electrochemical CO_2 reduction. J. Phys. Chem. C *122*, 3719–3726.

21. Heenen, H.H., Shin, H., Kastlunger, G., Overa, S., Gauthier, J.A., Jiao, F., and Chan, K. (2022). The mechanism for acetate formation in electrochemical CO_2 reduction on cu: selectivity with potential, ph, and nanostructuring. Energy Environ. Sci. *15*, 3978–3990.

22. Subramanian, S., Yang, K.L., Li, M.R., Sassenburg, M., Abdinejad, M., Irtem, E., Middelkoop, J., and Burdyny, T. (2023). Geometric catalyst utilization in zero-gap CO_2 electrolyzers. ACS Energy Lett. *8*, 222–229.

23. Li, P., Xing, C., Qu, S.J., Li, B., and Shen, W.Z. (2015). Carbon dioxide capturing by nitrogen-doping microporous carbon. ACS Sustainable Chem. Eng. *3*, 1434–1442.

24. Karapinar, D., Huan, N.T., Ranjbar Sahraie, N., Li, J., Wakerley, D., Touati, N., Zanna, S., Taverna, D., Galvão Tizei, L.H., Zitolo, A., et al. (2019). Electroreduction of CO_2 on single-site copper-nitrogen-doped carbon material: selective formation of ethanol and reversible restructuration of the metal sites. Angew. Chem. Int. Ed. *58*, 15098–15103.

25. Chen, C., Yan, X., Liu, S., Wu, Y., Wan, Q., Sun, X., Zhu, Q., Liu, H., Ma, J., Zheng, L., et al. (2020). Highly efficient electroreduction of CO_2 to C_{2+} alcohols on heterogeneous dual active sites. Angew. Chem. Int. Ed. Engl. *59*, 16459–16464.

26. Karapinar, D., Creissen, C.E., Rivera de la Cruz, J.G.R., Schreiber, M.W., and Fontecave, M. (2021). Electrochemical CO_2 reduction to ethanol with copper-based catalysts. ACS Energy Lett. *6*, 694–706.

27. Wang, X., Wang, Z.Y., García de Arquer, F.P.G., Dinh, C.T., Ozden, A., Li, Y.C., Nam, D.H., Li, J., Liu, Y.S., Wicks, J., et al. (2020). Efficient electrically powered CO_2-to-ethanol via suppression of deoxygenation. Nat. Energy *5*, 478–486.

28. Villholth, K.G., and Jensen, K.H. (1998). Flow and transport processes in a macroporous subsurface-drained glacial till soil II. Model analysis. J. Hydrol. *207*, 121–135.

29. Raimbault, J., Peyneau, P.E., Courtier-Murias, D., Bigot, T., Gil Roca, J.G., Béchet, B., and Lassabatère, L. (2021). Investigating the impact of exit effects on solute transport in macroporous media. Hydrol. Earth Syst. Sci. *25*, 671–683.

30. Thommes, M., Kaneko, K., Neimark, A.V., Olivier, J.P., Rodriguez-Reinoso, F., Rouquerol, J., and Sing, K. (2015). Physisorption of gases, with special reference to the evaluation of surface area and pore size distribution. Pure Appl. Chem. *87*, 9–10.

31. Gunathunge, C.M., Ovalle, V.J., Li, Y.W., Janik, M.J., and Waegele, M.M. (2018). Existence of an electrochemically inert CO population on cu electrodes in alkaline pH. ACS Catal. *8*, 7507–7516.

32. Gu, Z.X., Shen, H., Chen, Z., Yang, Y.Y., Yang, C., Ji, Y.L., Wang, Y.H., Zhu, C., Liu, J.L., Li, J., et al. (2021). Efficient electrocatalytic CO_2 reduction to C_{2+} alcohols at defect-site-rich cu surface. Joule *5*, 429–440.

33. Lum, Y., and Ager, J.W. (2018). Sequential catalysis controls selectivity in electrochemical CO_2 reudciton on Cu. Energy Environ. Sci. *11*, 2935–2944.

34. Fielicke, A., Gruene, P., Meijer, G., and Rayner, D.M. (2009). The adsorption of co on transition metal clusters: a case study of cluster surface chemistry. Surf. Sci. *603*, 1427–1433.

35. Krasser, W., Fadini, A., and Renouprez, A.J. (1980). The Raman spectrum of carbon monoxide chemisorbed on silica-supported nickel. J. Catal. *62*, 94–98.

36. Wang, X., Ou, P.F., Ozden, A., Hung, S.F., Tam, J., Gabardo, C.M., Howe, J.Y., Sisler, J., Bertens, K., García de Arquer, F.P.G., et al. (2022). Efficient electrosynthesis of n-propanol from carbon monoxide using a Ag-Ru-Cu catalyst. Nat. Energy *7*, 170–176.

37. Li, Y.C., Wang, Z.Y., Yuan, T.G., Nam, D.H., Luo, M.C., Wicks, J., Chen, B., Li, J., Li, F.W., de Arquer, F.P.G., et al. (2019). Binding site diversity promotes CO_2 electroreduction to ethanol. J. Am. Chem. Soc. *141*, 8584–8591.

38. Jouny, M., Luc, W., and Jiao, F. (2018). Author correction: high-rate electroreduction of carbon monoxide to multi-carbon products. Nat. Catal. *1*, 1002.

39. Bulushev, D.A., Chuvilin, A.L., Sobolev, V.I., Stolyarova, S.G., Shubin, Y.V., Asanov, I.P., Ishchenko, A.V., Magnani, G., Riccò, M., Okotrub, A.V., et al. (2017). Copper on carbon materials: stabilization by nitrogen doping. J. Mater. Chem. A *5*, 10574–10583.

40. Yamada, Y., Miyauchi, M., Kim, J., Hirose-Takai, K., Sato, Y., Suenaga, K., Ohba, T., Sodesawa, T., and Sato, S. (2011). Exfoliated graphene ligands stabilizing copper cations. Carbon *49*, 3375–3378.

41. Verma, S., Lu, S., and Kenis, P.J.A. (2019). Co-electrolysis of CO_2 and glycerol as a pathway to carbon chemicals with improved technoeconomics due to low electricity consumption. Nat. Energy *4*, 466–474.